

A SUBARU ARCHIVAL SEARCH FOR FAINT TRANS-NEPTUNIAN OBJECTS*

CESAR I. FUENTES AND MATTHEW J. HOLMAN

Harvard-Smithsonian Center for Astrophysics, 60 Garden Street, Cambridge, MA 02138, USA; cfuentes@cfa.harvard.edu
 Received 2008 February 28; accepted 2008 April 15; published 2008 May 27

ABSTRACT

We present the results of a survey for trans-Neptunian objects (TNOs) based on Subaru archival images, originally collected by Sheppard et al. in 2005 as part of a search for irregular satellites of Uranus. The survey region covers 2.8 deg^2 , centered on Uranus and observed near opposition on two adjacent nights. Our survey reaches half its maximum detection efficiency at $R = 25.69 \pm 0.01$. The objects detected correspond to 82 TNOs, five Centaurs, and five irregular satellites. We model the cumulative number of TNOs brighter than a given apparent magnitude with both a single power law (SPL) and a double power law (DPL). The best-fit SPL, with one object per square degree at magnitude $R_0 = 22.6^{+0.3}_{-0.4}$ and a slope of $\alpha = 0.51^{+0.5}_{-0.6}$, is inconsistent with the results of similar searches with shallower limiting magnitudes. The best-fit DPL, with a bright-end slope $\alpha_1 = 0.7^{+0.2}_{-0.1}$, a faint-end slope $\alpha_2 = 0.3^{+0.2}_{-0.1}$, a differential number density at $R = 23\sigma_{23} = 2.0^{+0.5}_{-0.5}$, and a magnitude break in the slope at $R_{\text{eq}} = 24.3^{+0.8}_{-0.1}$, is more likely than the SPL by a Bayes factor of ~ 26 . This is the first survey with sufficient depth and areal coverage to identify the magnitude at which the break occurs without relying on the results of other surveys. We estimate barycentric distances for the 73 objects that have 24 h arcs; only two have heliocentric distances as large as ~ 50 AU. We combine the distribution of observed distances with the size distribution that corresponds to a DPL luminosity function to set a tight constraint on the existence of a distant TNO population. We can exclude such a population at 60 AU, with 95% confidence, assuming it has the same size distribution and albedo as the observed TNOs, if it exceeds 8% of mass of the observed TNOs.

Key words: Kuiper Belt – solar system: formation

1. INTRODUCTION

The remnants of the protoplanetary disk, now in the form of trans-Neptunian objects (TNOs), offer a unique way to study the evolution of the solar system. The TNO size distribution is defined by its initial properties, collisional history, and the formation and evolution of the giant planets (Kenyon & Bromley 2004; Pan & Sari 2005; Kenyon et al. 2007). The orbital dynamics of the TNOs is largely governed by interactions with Neptune, and the radial distribution of TNOs also depends on the giant planets' evolution (see Morbidelli et al. 2007 for a review). It has been suggested that the radial extent of TNOs was truncated by the close passage of a star during the early stages of solar system formation (Brunini & Fernandez 1996; Ida et al. 2000; Kobayashi & Ida 2001; Kenyon & Bromley 2004).

A number of large-scale investigations that will significantly advance our understanding of the outer solar system are currently being designed, tested, and executed. Pan-STARRS (Jewitt 2003), given its coverage of the sky and time baseline, promises an accurate determination of the statistical properties of the trans-neptunian region. LSST (Tyson & Angel 2001) and SkyMapper (Keller et al. 2007) will extend the surveyed sky to the Southern Hemisphere. The New Horizons (NH) mission will give unprecedented views of the trans-Neptunian space by approaching Pluto and other TNOs in mid-2015. Nevertheless, there remain important questions that will not be answered by these studies. These large synoptic surveys will necessarily have a shallow limiting magnitude. Deep surveys like this will continue to be the only window into the smallest and farthest objects in the solar system. The answers to these questions can influence how these projects are carried out and how their

resulting data are interpreted. The distribution of faint objects will matter when large surveys choose fields to be covered more deeply. The TNO size distribution and radial extent of TNOs are among the questions that will rely on pencil-beam surveys to be answered.

Since the discovery of 1992 QB₁ (Jewitt et al. 1992) a number of wide-field surveys for TNOs have been completed (Jewitt et al. 1998; Chiang & Brown 1999; Larsen et al. 2001; Trujillo et al. 2001; Trujillo & Brown 2001; Millis et al. 2002; Trujillo & Brown 2003; Elliot et al. 2005; Larsen et al. 2007). In addition to determining much of the dynamical structure of the trans-Neptunian region and identifying large, bright TNOs that are amenable to follow-up observations, these surveys constrain the bright end ($R \lesssim 24$) of the cumulative luminosity function of TNOs, the number of objects per square degree brighter than a given magnitude. This quantity has consistently been measured to be a power law of the form

$$\Sigma(R) = 10^{\alpha(R-R_0)}, \quad (1)$$

where $R_0 \sim 23$ is the magnitude at which one expects one object per square degree and α is the slope of the distribution.

Ground-based efforts have also focused on detecting fainter TNOs with deeper imaging of narrow areas of the sky. Many have been successfully conducted in recent years (Gladman et al. 1998, 2001; Allen et al. 2001, 2002; Petit et al. 2004, 2006; Fraser et al. 2008). These surveys have been concentrated near the ecliptic plane and reach limiting magnitudes as faint as $R \sim 26$. These surveys also find that the cumulative surface density of TNOs is consistent with a single power law (SPL).

However, the deepest search to date, using the *Hubble Space Telescope* (HST) with the Advanced Camera for Surveys and reaching a 50% detection efficiency at magnitude $R = 28.5$, found 25 times fewer objects than expected from extrapolating the brighter ($R \lesssim 25$) distribution (Bernstein et al. 2004). Their

* Based on data collected at the Subaru Telescope, which is operated by the National Astronomical Observatory of Japan.

result indicates there is a break in the cumulative surface density of objects near $R \sim 25$.

Bernstein et al. (2004) necessarily relied upon the results of other surveys to assess the deviation of the cumulative density of objects from a SPL over a range of magnitudes. However, it is difficult to combine the results of different surveys to obtain a well-calibrated sample of the trans-Neptunian population.

Dynamical biases in latitude and longitude change the local density of objects and the relative abundances of excited and classical objects depending on the direction in which a survey is conducted. This can be seen in the variety of results found in the literature; a nice re-analysis and summary of some surveys is presented by Fraser et al. (2008). Different surveys sample a variety of ecliptic latitudes and longitudes, use various analysis methods, or vary in observing conditions. It is necessary to determine and correct for the effects of these differences to characterize the physical and dynamical properties of the TNO population. For bright TNOs, large synoptic surveys will determine many of the biases in the observations as well as in the population itself. However, for fainter TNOs, the simplest way to overcome these difficulties is to observe a single region of the sky.

All these surveys use the “digital tracking” method (Gladman & Kavelaars 1997; Gladman et al. 1998, 2001; Allen et al. 2001, 2002), by which a series of consecutive short exposures are digitally shifted and co-added to match the apparent motion of real objects. This method has proven very useful in improving the sensitivity of these ground- and space-based observations. However, it relies on how fine the grid of velocities sampled is, the good quality of a template image to subtract from each exposure, extra processing of the images and a trained operator to filter false positive detections due to saturated stars or other artifacts. Our results were obtained by linking detections in three different images described in Section 3. Our method’s data reduction is more direct, requires less human interaction and is easier to photometrically calibrate.

The radial extent of the classical TNO population is not known with certainty. Although there is evidence for a sudden decrease in density at $r \sim 50$ AU (Trujillo et al. 2001; Gladman et al. 2001), the existence of a second farther population near the ecliptic is difficult to rule out, due to the bias against detection of more distant, fainter objects. We are slightly more sensible to distant, slower moving objects. Since we do not rely on the construction of a template field, usually made with data taken on the same night, this increases the noise and would subtract signal from very slow movers.

The objectives of this work are to better constrain the expected break in the TNO luminosity function using a single survey and to better understand the lack of detections at large heliocentric distances. In the next section we describe the data and the processing of images. In Section 3 we present our moving object detection algorithm. We discuss the control population and detection efficiency of our method in Section 4. In the final two sections we present the results of our survey and discuss their implications for the size and distance distribution of the TNO population.

2. DATA

The observations considered in this project were taken on UT 2003 August 29 and 30 with Suprime-Cam (Miyazaki et al. 2002) mounted on the Subaru Telescope. Suprime-Cam is a mosaic camera with 10 CCDs, each with 2048×4096 pixels. Each mosaic image has a field of view (FOV) of $34' \times 27'$. We

used SMOKA, the electronic archive of the Subaru Telescope (Ichikawa 2002), to retrieve observations taken in 2003 August in the vicinity of Uranus, near opposition. The fields were originally observed by Sheppard et al. (2005). They surveyed a total of 14 fields, with an areal coverage of 3.57 deg^2 over the course of two nights. All exposures were taken with the “Cousins R” red filter, well matched to the colors of outer solar-system objects.

The objective of the original investigation was to discover Uranian irregular satellites. Sheppard et al. (2005) recovered all previously known Uranian irregular satellites and discovered two new such satellites. The faintest satellites detected have magnitudes at $R \sim 25.5$ (Sheppard et al. 2005; Kavelaars et al. 2004). On the first night, the observers took two or three exposures of ~ 7 min of each field, separated by half an hour on the first night. They re-observed those fields with two exposures during the second night, with the pointings shifted to maintain the same positions relative to Uranus. The survey was designed to discover objects during the first night and to obtain better orbital information using the second night’s data.

We chose this particular data set for the following reasons. The data set is sensitive to $R \lesssim 25.5$ mag objects, in the magnitude range in which Bernstein et al. (2004) find the break in the TNO cumulative function to be. This sensitivity is reached in a single exposure, avoiding the difficulties associated with combining different images. There are 11 fields (2.8 deg^2) with three exposures on the first night, permitting a simple search for moving objects. The fields were observed very close to opposition, allowing a reliable distance estimate from the rate of motion with only a 24 h arc. The sky coverage is large enough to expect the discovery of ~ 100 TNOs, allowing a significant constraint on the cumulative luminosity function. Finally, the data were easily obtained from the SMOKA system, after the 18 month proprietary period.

We performed the usual calibration of the images. For every image, we performed an overscan correction, trimming, bias frame subtraction, and flat-field division using standard IRAF¹ routines. Calibration frames taken during these observations were obtained from SMOKA.

3. MOVING OBJECT DETECTION

The apparent motion of outer solar-system objects viewed near opposition is primarily due to the Earth’s translation. For objects at the distance of Uranus the apparent motion can be as large as $\sim 6'' \text{ h}^{-1}$. For TNOs this rate is typically $\sim 3'' \text{ h}^{-1}$. This motion, with respect to background stars, is readily detected even in the short (~ 1 h) time baseline of this data set.

To find TNOs, Centaurs, and irregular satellites in this data set, we use a variant of the search algorithm described and implemented by Petit et al. (2004). This method is similar to that used in other TNO surveys (for example, Levison & Duncan 1990; Irwin et al. 1995; Jewitt & Luu 1995; Trujillo et al. 2001; Millis et al. 2002). The algorithm detects moving objects by comparing the positions of all point sources in each of three images of a patch of sky taken in the same night. Thus, as mentioned earlier, we restricted our search to the 11 fields for which there were three images taken on the first night. The individual steps in the algorithm are as follows.

¹ IRAF is distributed by the National Optical Astronomy Observatories, which are operated by the Association of Universities for Research in Astronomy, Inc., under cooperative agreement with the National Science Foundation.

First, for each search field we determine an astrometric solution for the first image of the night. These astrometric solutions are used later to guide the insertion of synthetic moving objects. We used the Two Micron All Sky Survey (2MASS) Point Source Catalog (Cutri et al. 2003) as an astrometric reference. The root mean square (rms) in the astrometric solution was typically of $0.2''$ or lower (close to the catalog's precision). The relative errors on the astrometric solutions for both nights were comparable to the tolerance of the search algorithm.

We then register the second and third images with the first image of the night. This allows for very accurate positioning of stellar-like objects with respect to each other. This is done for the individual CCDs, rather than for the entire mosaic. The successive CCD images are linearly interpolated, automatically, to the first using the positions of the background stars and routines available in the ISIS package (Alard 2000). When these routines fail to converge (due to numerous bad pixels or saturated stars), we align the images interactively using routines from IRAF.

At this stage, we insert the population of synthetic objects that will be used to determine the detection efficiency of the search, as described in Section 4.

We then use two different algorithms to search for point sources. The first of these is a wavelet transform source detection routine (see Petit et al. 2004 for a description). The second is the publicly available SExtractor package (Bertin & Arnouts 1996), which calculates the local image background rms, convolves the image with a user-specified kernel, and then identifies groups of pixels with values exceeding the background variation by a given value. These two approaches have very different false detection characteristics. Thus, we consider the intersection of detections from both routines. (We use the flux information given by SExtractor for the photometry described in Section 5.) We use a detection threshold of 2.6σ . For SExtractor this corresponds to four adjacent pixels with values that are at least 1.3 times of the local background variation. At the end of this stage, there are three lists of sources, one list for each image. This results in up to $\sim 50,000$ detections in each mosaic image. Note that the expected motion of TNOs during a single exposure (~ 7 min) is small compared to the typical FWHM ($0.7''$). Thus, trailing does not significantly affect the source detection.

In order to identify moving objects among all the point sources detected, we apply a series of filters that eliminate individual detections, as well as sequences of detections, that are not consistent with the TNO population.

We first reject all detections that corresponded to stationary objects, i.e. stars and galaxies. For each list of detections, we eliminate those for which there is a corresponding detection within $0.05''$ in at least one of the other two lists. We deliberately chose a small threshold in order not to diminish our sensitivity to very slow moving TNOs. This stage typically reduces the number of detections to $\sim 10,000$ per field.

The next step is to search for linear motion among the non-stationary detections. We identify all groups of three detections in the successive images that are consistent with straight line motion (within 15° of the ecliptic), with a constant angular rate between 0.5 and $10'' \text{ h}^{-1}$. The parameter space is chosen to include the expected rate and direction of TNOs. We consider all combinations of detections in the three different exposures whose fit to a line had an rms of $0.3''$ or less. These criteria are met by ~ 1600 combinations per field, nearly all of which are synthetic TNOs (see Section 4).

In the final stage, the search program outputs an image with all the combinations found, showing a stamp centered on every detection. We visually inspect these images to accept or reject a given object images. This method allows the spurious and acceptable detections to be rapidly distinguished (~ 30 min per field). Typically ~ 20 objects are rejected in this stage per field, the majority being optical artifacts, bad pixels, extended objects or some combination of the above.

4. CONTROL POPULATION AND DETECTION EFFICIENCY

Since our observations are flux limited it is necessary to account for detection biases when estimating the intrinsic number of TNOs as a function of magnitude. We characterize our search using a population of synthetic TNOs inserted just after the images have been calibrated and their astrometric solutions determined. The procedure is done for each mosaic field, rather than CCD by CCD. This process nicely accounts for the possible motion across detector boundaries. The same synthetic populations were used for the second night.

We used the *Orbfit* routines (Bernstein & Khushalani 2000) to create a realistic population of synthetic TNOs. The characteristics of the population were chosen to span the range of observational properties expected of the TNOs. The position of an object on the sky at the time of the first exposure was drawn from a uniform distribution that encompassed the FOV of the mosaic. Objects were implanted with distances between 20 AU and 200 AU, or alternatively $0.7'' \text{ h}^{-1}$ to $5.0'' \text{ h}^{-1}$. The proper motion and radial velocity given to the object are taken from a distribution that encompasses the possible rates found in the solar system. This initial position and velocity vectors are only accepted if they correspond to a bound orbit. If so, we use the *Orbfit* routines to calculate the right ascension (R.A.) and declination (decl.) of the object at the beginning and end times of each exposure. We translate these sky positions into locations on the mosaic using the astrometric solution derived earlier.

For each exposure we compute a model for the point-spread function (PSF). The model is the average of ~ 10 bright, isolated stars for every CCD. Given the known magnitude of the synthetic TNO and the measured zero point, and accounting for transparency changes through changes in the flux measured in the PSF stars, we use IRAF routines to insert PSFs with this flux at the calculated positions. We inserted objects from 22.5 to 26.5 mag, which spans the magnitudes of the TNO population we expect to find. The flux of each object includes photon noise. We did not consider variable objects, as this is unlikely to be significant on ~ 1 h timescales. We include the effect of trailing by dividing the flux among several PSFs inserted at positions linearly interpolated between those at the beginning and end of the exposures. This process takes into account any background, transparency, seeing, and focus variations that might affect the limiting magnitude. Using this PSF model from each image, we implant a set of ~ 2000 objects per field. This results in a sufficient number of synthetic objects per CCD to sample the detection efficiency as a function of position.

Since we count objects up to a certain brightness and our model describes the underlying TNO population, it is essential to estimate what fraction of the population we detect as a function of magnitude. In Figure 1 we include a histogram of the fraction of objects that were recovered in each magnitude bin. We implanted 25,074 objects in 11 fields, recovering 17,195 of them.

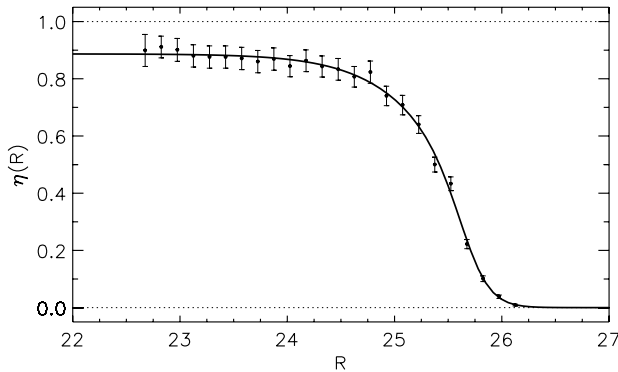


Figure 1. Detection efficiency as a function of magnitude, with an error given by the number of objects implanted and found in each bin. The fitted curve corresponds to Equation (2), where the best-fit values are $A = 0.88 \pm 0.01$, $R_{50} = 25.69 \pm 0.01$, $w_1 = 0.28 \pm 0.04$, and $w_2 = 0.88 \pm 0.15$. R_{50} corresponds to the magnitude at which our method is 50% as efficient as its maximum detection efficiency.

When plotting the cumulative function we used the local efficiency function, each detection is weighed by the number of objects recovered in the same field and within the observational magnitude error. The detection efficiency could vary from field to field. Since all fields were taken in the vicinity of Uranus, efficiency could depend on location. However, its statistical effect on the efficiency was negligible.

For the statistical analysis the effective efficiency function will need to be integrated. Since it is simpler to integrate analytical expressions, we used the total efficiency function that considers all fields. Following Petit et al. (2006), we represent it by

$$\eta(R) = \frac{A}{4} \left(1 - \tanh \frac{R - R_{50}}{w_1} \right) \left(1 - \tanh \frac{R - R_{50}}{w_2} \right), \quad (2)$$

where the best-fit values are $A = 0.88 \pm 0.01$, $R_{50} = 25.69 \pm 0.01$, $w_1 = 0.28 \pm 0.04$, and $w_2 = 0.88 \pm 0.15$. The errors were obtained with a Markov Chain Monte Carlo simulation. The parameter A corresponds to the maximum efficiency, achieved for bright objects. R_{50} corresponds to the magnitude at which the detection efficiency drops to half the maximum values. The parameters w_1 and w_2 characterize the abruptness of the decline of the detection efficiency. Figure 1 shows the average efficiency function for our data set.

The efficiency could also depend on the rate of motion. We construct a rate analog to the magnitude efficiency (see Figure 2). The detection efficiency is nearly independent of rate, but our method is slightly less efficient at larger rates. A faster-moving object that is detected in the first image has a greater chance of falling close to a background star, or moving outside the FOV; thus the detection efficiency declines with the rate of motion. The lowest bin plot in Figure 2 is $1.5'' \text{ h}^{-1}$. Since we implanted objects to have a population with a constant surface density that bin is not well sampled. Even though we were able to recover objects planted with rates as slow as $0.7'' \text{ h}^{-1}$ (parallax for objects at 200 AU) we consider a more conservative limit. The rate at which an object moves one FWHM in 45 min, the shortest separation between the first and third exposures, is $0.9'' \text{ h}^{-1}$ (150 AU).

To properly account for detection biases, both real and control objects must go through exactly the same validation procedure. We did not unveil the fake object list until all objects were recognized as moving objects, either real or planted.

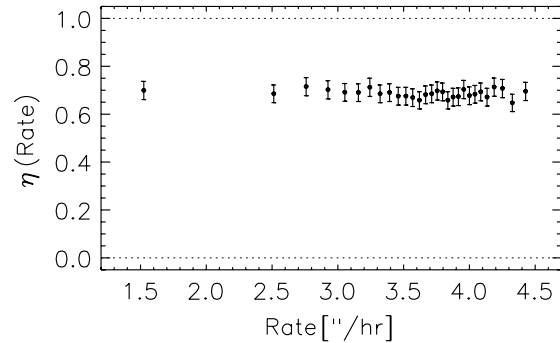


Figure 2. Histogram of the fraction of objects recovered as a function of rate. Bins are chosen to have similar numbers of objects. This demonstrates that our detection efficiency does not depend significantly upon the rate of motion.

5. RESULTS AND ANALYSIS

We found 92 moving objects, five corresponding to known irregular Uranian satellites (those found by Kavelaars et al. 2004 and Sheppard et al. 2005), five to Centaurs, and 82 to TNOs. The satellites that were missed were blended with stars in one of the images and hence were not found by our algorithm.

We present our detections in Table 1. For each TNO, we list its internal designation, its position at the time of the first exposure (also listed), and its estimated magnitude with uncertainties (along with an independent estimate of the photometric uncertainty). We also list the measured sky plane rates of motion of the TNO, two estimates of the distance to the TNO (one suited for two nights' data and another based only on parallax, both explained later), its orbital inclination, and separation from Uranus at the time of discovery.

Three standard stars (Landolt 1992) were used to obtain the zero point and airmass dependence of the photometry. These were PG2213-006C ($V = 15.11 \pm 0.0045$, $V - R = 0.426 \pm 0.0023$) SA-92-417 ($V = 15.92 \pm 0.0127$, $V - R = 0.351 \pm 0.0151$) and SA-92-347 ($V = 15.75 \pm 0.0255$, $V - R = 0.339 \pm 0.0295$). Since their colors are similar to those of typical TNOs (Peixinho et al. 2004) we did not apply a color correction. We checked both nights were photometric and stable. The possible dependence on seeing (FWHM) was also investigated, finding it to be unimportant. The correction term was negligible compared to the airmass correction. Every detection's magnitude was calculated, using the following formula:

$$R = 27.36 - 2.5 \log f_5/t - 0.09X, \quad (3)$$

where f_5 corresponds to the flux in a five-pixel aperture, t is the time in seconds and X is the airmass. This equation accounts for an average 0.34 mag aperture correction between the known magnitude of a synthetic object and its magnitude measured with a five-pixel aperture. The search algorithm requires an object to be found in all three exposures giving three independent magnitude measurements that we average to obtain the results shown in Table 1. The errors given on the magnitude values correspond to the error on the flux.

In Figure 3 we plot the photometric errors, showing them to be ~ 0.1 mag. The magnitude dependence of the uncertainty is shown in Figure 4. We estimate the uncertainties empirically, calculating the standard deviation as a function of magnitude. We then fit a second-degree polynomial, overlaid in Figure 4. This estimate is shown for each real object as $\Delta_{R_{\text{mag}}}$ in Table 1.

Table 1
Fit Parameters^a

Name	MJD	R.A.	Decl.	R_{mag}	ΔR_{mag}	$dR.A./dt$ (" h ⁻¹)	$d\text{Decl.}/dt$ (" h ⁻¹)	d_{par} (AU)	d_{bari} (AU)	i (deg)	$\Delta_{\alpha}(\text{Uranus})$ (')
sukbo88	52880.456823	22:09:09.42	-12:46:24.35	23.57 ^{+0.05} _{-0.05}	0.07	-2.81	-1.04	43.0	42.9 ± 2.5	2.2 ± 1.1	60
sukbo57	52880.387131	22:09:15.90	-11:55:25.85	24.97 ^{+0.13} _{-0.15}	0.14	-2.78	-1.02	43.4	43.2 ± 2.5	0.7 ± 0.8	38
sukbo17	52880.467440	22:09:24.36	-11:37:45.60	25.03 ^{+0.14} _{-0.16}	0.14	-2.67	-1.01	45.2	44.9 ± 2.5	2.7 ± 1.6	42
sukbo23	52880.467440	22:09:26.17	-11:16:08.70	24.25 ^{+0.10} _{-0.11}	0.10	-2.68	-0.90	46.0	45.5 ± 2.6	9.4 ± 3.6	56
sukbo59	52880.387131	22:09:33.47	-11:52:17.45	25.47 ^{+0.16} _{-0.19}	0.17	-2.82	-1.04	42.9	42.6 ± 2.5	1.0 ± 1.1	34
sukbo52	52880.387131	22:09:36.21	-12:06:01.14	23.75 ^{+0.04} _{-0.04}	0.08	-2.58	-0.96	47.0	46.9 ± 2.5	1.6 ± 1.3	33
sukbo90	52880.456823	22:09:38.29	-12:39:41.88	25.60 ^{+0.19} _{-0.23}	0.17	-2.95	-1.09	40.8	40.6 ± 2.5	1.7 ± 0.8	51
sukbo24	52880.467440	22:09:40.30	-11:12:11.25	24.54 ^{+0.12} _{-0.13}	0.12	-2.70	-1.00	44.8	44.5 ± 2.5	0.5 ± 1.2	58
sukbo51	52880.387131	22:09:45.05	-12:08:45.55	24.37 ^{+0.08} _{-0.08}	0.11	-3.05	-1.11	39.5	39.2 ± 2.4	1.0 ± 0.7	31
sukbo50	52880.387131	22:09:47.61	-12:10:06.91	25.13 ^{+0.15} _{-0.17}	0.15	-2.73	-0.98	44.6	44.3 ± 2.5	2.4 ± 1.4	31
sukbo54	52880.387131	22:09:48.36	-12:05:40.42	25.59 ^{+0.20} _{-0.25}	0.17	-2.68	-0.99	45.2	45.0 ± 2.5	1.5 ± 1.2	30
sukbo22	52880.467440	22:09:51.25	-11:21:10.92	24.74 ^{+0.13} _{-0.15}	0.13	-2.36	-1.02	50.8	50.8 ± 2.8	18.4 ± 7.0	49
sukbo55	52880.387131	22:09:51.26	-12:03:05.07	24.63 ^{+0.12} _{-0.14}	0.12	-2.69	-1.03	44.7	44.6 ± 2.5	4.2 ± 1.9	29
sukbo48	52880.387131	22:09:53.94	-12:16:51.14	25.52 ^{+0.17} _{-0.20}	0.17	-3.13	-1.54	37.6	37.9 ± 3.3	34.6 ± 16.4	32
sukbo60 ^b	52880.387131	22:09:55.42	-11:50:18.49	25.77 ^{+0.19} _{-0.23}	0.19	-2.82	-1.03	42.9	46.4 ± 12.0	^c	29
sukbo58 ^b	52880.387131	22:10:01.46	-11:52:42.62	25.68 ^{+0.20} _{-0.25}	0.18	-2.85	-0.86	44.3	47.5 ± 11.1	^c	27
sukbo91	52880.456823	22:10:26.15	-12:35:13.32	24.36 ^{+0.07} _{-0.08}	0.11	-2.76	-1.06	43.5	43.4 ± 2.5	5.0 ± 2.0	40
sukbo21	52880.467440	22:10:27.48	-11:26:00.88	23.72 ^{+0.06} _{-0.06}	0.07	-2.79	-1.06	43.1	42.9 ± 2.5	3.2 ± 1.6	40
sukbo16	52880.467440	22:10:30.60	-11:41:46.06	23.31 ^{+0.04} _{-0.05}	0.06	-2.82	-1.00	43.2	42.8 ± 2.5	3.9 ± 1.8	27
sukbo53	52880.387131	22:10:31.56	-12:06:20.06	24.52 ^{+0.08} _{-0.09}	0.11	-2.57	-0.95	47.2	47.0 ± 2.5	0.8 ± 0.1	20
sukbo56	52880.387131	22:10:32.98	-12:02:16.43	23.95 ^{+0.05} _{-0.05}	0.09	-2.67	-1.01	45.2	45.2 ± 2.5	3.9 ± 1.8	18
sukbo93	52880.456823	22:10:36.60	-12:18:23.83	23.97 ^{+0.08} _{-0.09}	0.09	-2.69	-1.00	44.9	44.8 ± 2.5	1.5 ± 1.1	25
sukbo92	52880.456823	22:10:39.91	-12:26:38.52	25.38 ^{+0.21} _{-0.27}	0.16	-2.87	-1.07	42.0	41.8 ± 2.5	2.7 ± 1.3	31
sukbo94	52880.456823	22:10:42.50	-12:18:33.94	23.85 ^{+0.07} _{-0.07}	0.08	-2.79	-1.01	43.5	43.3 ± 2.5	1.7 ± 1.1	24
sukbo45	52880.348317	22:10:51.30	-12:36:53.32	24.15 ^{+0.06} _{-0.07}	0.10	-2.92	-1.09	41.2	41.1 ± 2.5	2.3 ± 1.0	39
sukbo49 ^b	52880.387131	22:10:52.67	-12:13:42.84	25.41 ^{+0.17} _{-0.20}	0.16	-2.89	-0.95	42.6	46.8 ± 12.0	^c	19
sukbo0	52880.337272	22:10:52.89	-12:13:41.26	25.23 ^{+0.15} _{-0.18}	0.15	-2.84	-1.03	42.7	42.5 ± 2.5	1.3 ± 0.8	19
sukbo61 ^b	52880.387131	22:10:53.87	-11:45:27.66	23.13 ^{+0.03} _{-0.03}	0.05	-2.88	-1.08	41.7	43.1 ± 9.8	^c	20
sukbo31	52880.342793	22:10:54.08	-11:45:26.57	23.19 ^{+0.03} _{-0.03}	0.05	-2.84	-1.06	42.4	42.2 ± 2.5	1.2 ± 1.1	20
sukbo2	52880.337272	22:10:54.93	-12:12:09.59	25.64 ^{+0.19} _{-0.24}	0.18	-2.72	-1.05	44.2	44.2 ± 2.5	6.1 ± 2.4	17
sukbo44	52880.348317	22:10:57.80	-12:42:51.61	25.25 ^{+0.14} _{-0.16}	0.15	-3.11	-1.25	38.2	38.1 ± 2.5	9.8 ± 3.7	44
sukbo34	52880.342793	22:11:03.64	-11:31:33.24	24.17 ^{+0.07} _{-0.07}	0.10	-2.77	-1.03	43.5	43.3 ± 2.5	0.9 ± 1.1	31
sukbo27	52880.472734	22:11:04.46	-13:09:42.98	25.16 ^{+0.14} _{-0.16}	0.15	-2.94	-1.09	41.0	41.0 ± 2.5	2.7 ± 0.9	70
sukbo73	52880.397724	22:11:06.70	-10:54:01.82	24.96 ^{+0.13} _{-0.15}	0.14	-2.65	-1.01	45.5	45.3 ± 2.5	2.3 ± 1.5	67
sukbo46	52880.348317	22:11:09.54	-12:35:08.71	24.58 ^{+0.10} _{-0.10}	0.12	-2.59	-0.99	46.6	46.7 ± 2.5	5.5 ± 2.2	36
sukbo25	52880.472734	22:11:15.88	-13:17:16.77	24.95 ^{+0.17} _{-0.21}	0.14	-3.13	-1.24	37.9	38.0 ± 2.5	8.6 ± 3.1	77
sukbo39	52880.348317	22:11:17.04	-12:51:56.40	25.37 ^{+0.17} _{-0.20}	0.16	-2.79	-1.04	43.2	43.2 ± 2.5	2.3 ± 1.0	52
sukbo8	52880.337272	22:11:20.06	-12:03:12.63	25.13 ^{+0.13} _{-0.15}	0.15	-2.80	-1.05	43.1	42.9 ± 2.5	1.7 ± 1.1	7
sukbo6	52880.337272	22:11:23.29	-12:05:17.03	25.80 ^{+0.21} _{-0.27}	0.19	-2.83	-1.02	42.9	42.7 ± 2.5	1.7 ± 1.1	7
sukbo33	52880.342793	22:11:24.19	-11:37:12.39	24.19 ^{+0.06} _{-0.07}	0.10	-2.96	-1.06	40.8	40.6 ± 2.5	2.8 ± 1.4	24
sukbo43	52880.348317	22:11:24.34	-12:48:33.44	25.18 ^{+0.16} _{-0.20}	0.15	-2.84	-1.29	41.7	42.1 ± 2.9	25.5 ± 10.3	48
sukbo3	52880.337272	22:11:26.81	-12:11:39.44	25.60 ^{+0.18} _{-0.22}	0.18	-2.75	-1.04	43.8	43.7 ± 2.5	3.2 ± 1.5	12
sukbo42	52880.348317	22:11:37.53	-12:49:36.33	24.55 ^{+0.10} _{-0.11}	0.12	-2.87	-1.03	42.3	42.1 ± 2.5	2.6 ± 1.1	49
sukbo77	52880.397724	22:11:47.57	-10:51:02.90	23.34 ^{+0.03} _{-0.03}	0.06	-2.83	-1.06	42.5	42.2 ± 2.5	1.0 ± 1.1	69
sukbo32	52880.342793	22:11:47.88	-11:38:28.77	24.70 ^{+0.09} _{-0.10}	0.12	-2.79	-1.07	43.1	43.0 ± 2.5	3.7 ± 1.7	22
sukbo1	52880.337272	22:11:49.55	-12:12:54.47	25.62 ^{+0.18} _{-0.22}	0.18	-2.78	-1.05	43.3	43.3 ± 2.5	3.1 ± 1.4	13
sukbo5	52880.337272	22:11:51.99	-12:07:17.95	24.27 ^{+0.07} _{-0.07}	0.10	-2.89	-1.07	41.6	41.5 ± 2.5	1.2 ± 0.8	7
sukbo37 ^b	52880.342793	22:11:53.44	-11:26:56.13	25.65 ^{+0.21} _{-0.26}	0.18	-2.38	-0.59	60.1	^c	^c	34
sukbo4	52880.337272	22:11:53.69	-12:10:54.32	24.46 ^{+0.08} _{-0.08}	0.11	-3.19	-1.54	36.7	36.9 ± 3.0	29.8 ± 13.2	11
sukbo13	52880.337272	22:12:00.29	-11:59:26.11	25.37 ^{+0.17} _{-0.21}	0.16	-2.81	-1.38	42.1	42.4 ± 3.4	35.2 ± 16.2	4
sukbo38	52880.342793	22:12:08.82	-11:16:55.93	25.29 ^{+0.15} _{-0.18}	0.16	-2.51	-0.76	50.6	50.0 ± 2.8	21.0 ± 8.0	44
sukbo28	52880.472734	22:12:21.36	-13:01:26.73	23.39 ^{+0.05} _{-0.05}	0.06	-2.77	-1.03	43.6	43.6 ± 2.5	2.6 ± 1.0	62
sukbo78	52880.397724	22:12:21.47	-10:42:48.31	22.64 ^{+0.02} _{-0.02}	0.03	-2.78	-1.10	43.0	42.9 ± 2.5	6.6 ± 2.7	78

Table 1
(Continued)

Name	MJD	R.A.	Decl.	R_{mag}	ΔR_{mag}	$dR.A./dt$ (" h ⁻¹)	$d\text{Decl.}/dt$ (" h ⁻¹)	d_{par} (AU)	d_{bari} (AU)	i (deg)	$\Delta_{\alpha}(\text{Uranus})$ (')
sukbo74	52880.397724	22:12:27.15	-10:52:56.00	22.99 ^{+0.02} _{-0.02}	0.04	-2.72	-1.00	44.5	44.3 ± 2.5	1.7 ± 1.3	68
sukbo76	52880.397724	22:12:27.37	-10:51:42.55	25.49 ^{+0.17} _{-0.21}	0.17	-2.86	-1.10	41.9	41.6 ± 2.5	3.1 ± 1.6	69
sukbo26	52880.472734	22:12:27.91	-13:17:09.62	25.17 ^{+0.17} _{-0.20}	0.15	-2.86	-1.12	41.8	41.8 ± 2.5	7.8 ± 2.8	77
sukbo75	52880.397724	22:12:28.22	-10:51:23.92	25.59 ^{+0.17} _{-0.20}	0.17	-2.84	-0.84	44.7	44.1 ± 2.8	23.3 ± 9.3	70
sukbo41	52880.348317	22:12:28.24	-12:50:19.12	24.92 ^{+0.13} _{-0.15}	0.14	-2.95	-1.14	40.5	40.5 ± 2.5	5.4 ± 2.0	51
sukbo29	52880.472734	22:12:28.90	-13:00:29.66	23.86 ^{+0.06} _{-0.07}	0.08	-2.91	-1.07	41.4	41.4 ± 2.5	1.9 ± 0.5	61
sukbo35	52880.342793	22:12:32.78	-11:31:13.39	25.58 ^{+0.17} _{-0.20}	0.17	-2.72	-1.25	43.5	43.6 ± 2.9	25.3 ± 10.3	31
sukbo99	52880.462148	22:12:40.64	-12:27:42.77	24.28 ^{+0.09} _{-0.09}	0.10	-2.76	-1.01	43.9	43.8 ± 2.5	1.3 ± 0.1	31
sukbo47 ^b	52880.348317	22:12:41.16	-12:27:39.37	23.89 ^{+0.05} _{-0.05}	0.08	-2.81	-1.07	42.8	^c	^c	31
sukbo81	52880.403236	22:12:54.24	-11:39:25.88	25.26 ^{+0.15} _{-0.18}	0.16	-3.06	-1.34	38.5	38.5 ± 2.6	18.1 ± 7.1	27
sukbo69	52880.392433	22:13:01.10	-11:52:24.31	25.26 ^{+0.15} _{-0.18}	0.16	-2.98	-1.10	40.4	40.3 ± 2.4	0.8 ± 0.3	20
sukbo67	52880.392433	22:13:02.05	-12:08:55.50	24.66 ^{+0.09} _{-0.10}	0.12	-2.88	-1.04	42.1	41.9 ± 2.5	2.0 ± 1.1	21
sukbo64	52880.392433	22:13:07.07	-12:12:25.08	24.48 ^{+0.08} _{-0.09}	0.11	-2.92	-1.11	41.0	41.0 ± 2.5	2.6 ± 1.2	24
sukbo85	52880.403236	22:13:16.86	-11:25:45.74	24.20 ^{+0.06} _{-0.07}	0.10	-2.76	-1.04	43.7	43.6 ± 2.5	1.9 ± 1.3	41
sukbo63	52880.392433	22:13:18.02	-12:13:17.31	25.37 ^{+0.16} _{-0.19}	0.16	-2.81	-1.05	42.9	42.9 ± 2.5	1.9 ± 1.0	26
sukbo65	52880.392433	22:13:25.44	-12:09:50.02	25.52 ^{+0.16} _{-0.19}	0.17	-2.69	-1.00	45.0	44.9 ± 2.5	1.6 ± 1.0	27
sukbo87 ^b	52880.403236	22:13:26.02	-11:17:06.76	25.27 ^{+0.15} _{-0.18}	0.16	-2.62	-0.94	46.5	^c	^c	50
sukbo96	52880.462148	22:13:28.31	-12:42:21.29	25.40 ^{+0.21} _{-0.26}	0.16	-2.74	-0.98	44.4	44.2 ± 2.5	3.3 ± 1.4	49
sukbo100	52880.462148	22:13:39.25	-12:26:53.85	24.31 ^{+0.08} _{-0.09}	0.10	-2.99	-1.05	40.6	40.4 ± 2.5	4.3 ± 1.8	39
sukbo62 ^b	52880.392433	22:13:42.77	-12:15:37.04	25.16 ^{+0.13} _{-0.14}	0.15	-2.01	-1.34	60.1	65.2 ± 17.4	^c	33
sukbo72	52880.392433	22:13:51.41	-11:46:46.76	25.14 ^{+0.14} _{-0.17}	0.15	-2.81	-1.05	42.9	42.8 ± 2.5	1.0 ± 0.7	34
sukbo80	52880.403236	22:13:56.31	-11:40:41.22	25.38 ^{+0.18} _{-0.22}	0.16	-2.70	-1.02	44.7	44.6 ± 2.5	1.8 ± 1.2	38
sukbo86	52880.403236	22:13:58.17	-11:23:21.45	24.94 ^{+0.12} _{-0.14}	0.14	-3.13	-0.99	39.5	39.1 ± 2.5	14.8 ± 5.8	50
sukbo79	52880.403236	22:13:59.82	-11:41:10.37	24.61 ^{+0.14} _{-0.17}	0.12	-3.06	-1.19	39.0	38.9 ± 2.4	4.7 ± 1.9	39
sukbo95	52880.462148	22:14:02.62	-12:47:04.86	24.71 ^{+0.14} _{-0.16}	0.12	-2.81	-1.02	43.1	43.1 ± 2.5	1.7 ± 0.3	58
sukbo70	52880.392433	22:14:06.42	-11:48:59.37	25.04 ^{+0.12} _{-0.14}	0.14	-2.76	-1.04	43.6	43.5 ± 2.5	2.1 ± 1.2	37
sukbo71	52880.392433	22:14:13.53	-11:47:47.21	24.25 ^{+0.08} _{-0.09}	0.10	-3.00	-1.09	40.2	40.0 ± 2.4	1.9 ± 1.1	39
sukbo97	52880.462148	22:14:13.95	-12:38:36.76	24.73 ^{+0.12} _{-0.13}	0.13	-2.84	-1.06	42.4	42.4 ± 2.5	2.1 ± 0.8	53
sukbo66 ^b	52880.392433	22:14:22.17	-12:09:05.58	25.01 ^{+0.13} _{-0.15}	0.14	-3.32	-1.65	35.2	34.9 ± 7.5	^c	40

Notes.

^a All 82 TNOs found. The second night data were used when possible. The measured magnitude in the R filter with nominal errors is shown in R_{mag} . ΔR_{mag} is a model for the photometric error based on the measure magnitudes of inserted, synthetic objects. $dR.A./dt$ and $d\text{Decl.}/dt$ are estimates of the measured motion of the object. The distance d_{par} is calculated with the assumption of a circular orbit. d_{bari} is the barycentric distance estimate and i is the inclination estimate given by the *Orbfit* code (Bernstein & Khushalani 2000). $\Delta_{\alpha}(\text{Uranus})$ is the projected distance to Uranus during the observations.

^b These objects were not found in the second night of observations.

^c The result is unconstrained.

We can accurately approximate the apparent motion of a TNO over 24 h as a straight line with a constant rate. We include the measured R.A. and decl. rates in Table 1. The apparent motion of our objects compared with that which parallels the ecliptic is plotted in Figure 5.

Near opposition, the change in the rate or direction of motion over 24 h is negligible, making it easy to predict where the real objects would be on the second night. However, nine objects were not found on the second night. Our method is only ~90% efficient for the brightest objects on the first night, with 10% lost to blending with field stars. It is expected that more than 10% of the objects will be lost on the second night, because of confusion with stationary sources and because they are more likely to move outside the FOV over 24 h.

We used the observations on the second night to improve the distance determination when possible. We use the Bernstein & Khushalani (2000) *Orbfit* routines to estimate plausible orbital elements assuming there is no acceleration in the direction

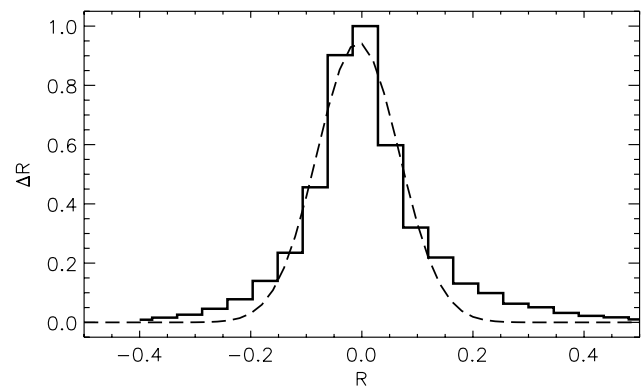


Figure 3. Histogram of the magnitude error (ΔR) as a function of R magnitude for all implanted objects. The error is defined as the difference between the implanted and measured magnitudes for the synthetic population. The dashed line is a Gaussian of width ~0.1 mag.

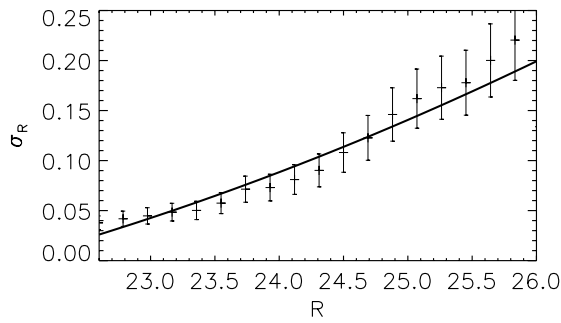


Figure 4. The error in magnitude for synthetic objects as a function of magnitude is shown for different magnitude bins. The error is defined as the FWHM of the best-fit Gaussian to the histogram of errors for all objects in each bin. The error bars correspond to the calculated uncertainty of the FWHM. The curve is a quadratic fit to the data and defines the error estimate used for ΔR_{mag} in Table 1.

tangential to the plane of the sky. For a 24 h arc, this results in a $\sim 7\%$ accuracy in the barycentric distance (d_{bari}). For a single night observation of objects the error on the distance could be unbound. However, since the observations were taken near opposition we are able to readily estimate heliocentric distances (d_{par}) from the “parallactic motion.” We assume that the observations are taken exactly at opposition and that the orbits are circular. This distance estimate is not as reliable as d_{bari} but it serves as a consistency check.

5.1. Statistical Analysis

The probability of our data (D) given a model for the intrinsic population (M) is denoted $P(D|M) = L(M)$, where L is the likelihood function. We consider the data in our survey as a collection of N detections with measured magnitudes. As derived in Schechter & Press (1976) if $g(m)dm$ is the expected number of detections between m and $m+dm$, then the likelihood of a set m_i where $i = 1, \dots, N$ is

$$L(M) = \exp \left[- \int_{-\infty}^{\infty} g(m) dm \right] \prod_{i=1}^N g(m_i) dm. \quad (4)$$

We are interested in characterizing $g(m)$. As described in Bernstein et al. (2004), we can think of $g(m)$ as being the probability of detecting an object and assigning it a magnitude m given the survey characteristics and the real distribution of objects on the sky. We consider an intrinsic differential surface density of objects σ that only depends on magnitude and is constant over the observed area as the model M . For a survey with an efficiency function η , a function of magnitude only, we can write $\int_{-\infty}^{\infty} g(m) dm = \Omega \int \eta(m) \sigma(m) dm$, where Ω is the solid angle of the survey.

The likelihood of a model for the differential surface density $\sigma(m)$ is then given by

$$L(\sigma) = e^{-\Omega \int \eta(m) \sigma(m) dm} \prod_i \int l_i(m) \eta(m) \sigma(m) dm. \quad (5)$$

This is the probability of finding each object in the set of observations at its measured magnitude, scaled by the probability of not finding anything else. The function $l_i(m)$ is the probability an object is given a magnitude m_i given its intrinsic magnitude is m .

If we consider the efficiency function and model it as relatively linear over the magnitude uncertainty of an observation

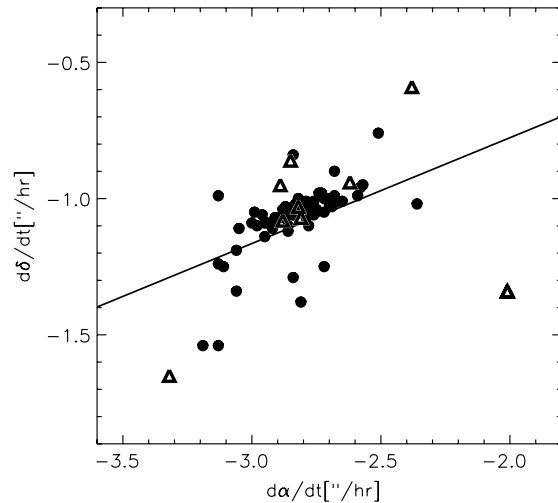


Figure 5. Rate of motion in the sky for every TNO. Objects observed on one night only are represented by triangles. The ecliptic motion is overplotted as a solid line.

we can approximate our likelihood function as follows:

$$L(\sigma) = e^{-\Omega \int \eta(x) \sigma(x) dx} \prod_i \eta(m_i) \sigma(m_i). \quad (6)$$

This is extremely useful when dealing with a large number of objects and surveys. We compared the behavior of both exact and approximate likelihood functions with our data and found no noticeable differences.

If we want to sample the likelihood function over its parameter space or calculate the total likelihood of a model we need to consider priors, that is, the probability of a parameter q given a certain model M , $P(q|M)$. These priors reflect any knowledge we have over the value of a parameter previous to our survey. We chose priors that reflect the least previous knowledge into the analysis. We chose uniform functions between limits set by our survey, indicating our ignorance of those parameters. The total probability of a model is

$$\mathcal{L}(\sigma) = \int P(q|\sigma) L(\sigma, q) dq. \quad (7)$$

We can compare two competing models using their total likelihoods by computing the odds ratio:

$$O_{21} = \frac{P(\sigma_2|D)}{P(\sigma_1|D)} = \frac{P(\sigma_2)}{P(\sigma_1)} \frac{P(D|\sigma_2)}{P(D|\sigma_1)} = \frac{\mathcal{L}(\sigma_2)}{\mathcal{L}(\sigma_1)}. \quad (8)$$

The last equality holds if we do not have a good reason to prefer “*a priori*” any of the two models. The ratio of the total likelihoods is called the Bayes factor.

5.2. Single Power Law Model

One of our goals is to determine whether the results of our survey indicate that the cumulative surface density can be modeled by an SPL distribution or if the data favor a more complicated model. We use a likelihood analysis to investigate this.

The likelihood function is related to both the detection efficiency of the survey and the differential surface density $\sigma(R)$. The important observation for the analysis is the number of

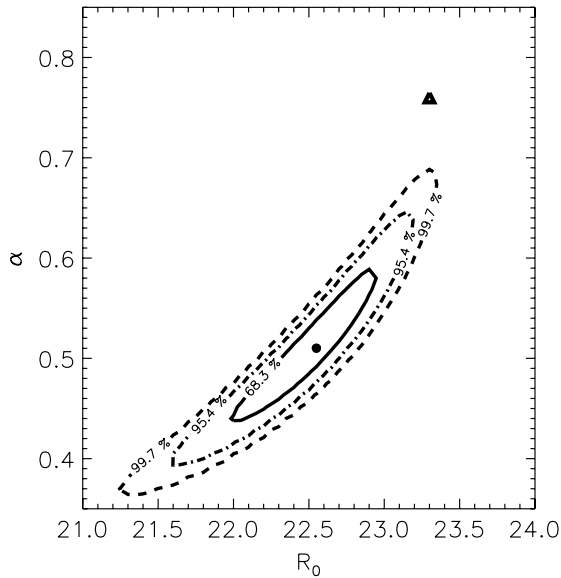


Figure 6. Contours of the SPL likelihood function. The maximum likelihood point is marked with a dot ($\alpha = 0.51$, $R_0 = 22.6$). Marked with a triangle is the best value for the parameters based on Petit et al. (2006) ($\alpha = 0.76$, $R_0 = 23.3$). This shows the discrepancy between our result and that of Petit et al. (2006).

objects we detect brighter than a given magnitude, namely the cumulative surface density: $\Sigma(R) = \int_{-\infty}^R \sigma(x) dx$. We use the likelihood function given by Equation (5), with $\Omega = 2.83 \text{ deg}^2$ and $\eta(R)$ given by Equation (2).

For every object we model its photometric uncertainty using the analytical model we considered previously, a Gaussian (l_i) around its measured magnitude (see Figure 4).

The SPL model is written as follows:

$$\sigma_1(R, \alpha, R_0) = \alpha \ln(10) 10^{\alpha(R-R_0)}. \quad (9)$$

In Figure 6 we plot the SPL likelihood as a function of R_0 and α . The previously accepted values for the SPL parameters ($\alpha = 0.76$, $R_0 = 23.3$) (Petit et al. 2006) are in strong disagreement with our data, lying well outside our 3σ confidence region. Most of the surveys that have consistently measured a slope of $\alpha \sim 0.7$ for the cumulative distribution have brighter limiting magnitudes (Gladman et al. 1998; Petit et al. 2004, 2006). The exceptions are Gladman et al. (2001) and Fraser et al. (2008), who quote a magnitude limit of $R = 25.9$ and $R = 25.6$, respectively. Bernstein et al. (2004) performed a search complete to $R = 28.5$. They discovered far too few objects to be consistent with an SPL.

We check that our bright-end sample is consistent with the previous surveys with shallower limiting magnitudes. In Figure 7 we plot our sample's likelihood function after imposing an artificial efficiency limit at $R = 24.5$. The power-law index is clearly consistent with the Petit et al. (2006) result and it shows that our sample does not deviate from the SPL behavior observed by others for magnitudes brighter than $R \sim 24.5$.

To show that the deviation from an SPL at fainter magnitudes is not an artifact of our efficiency function, we repeated the experiment but instead imposed an artificial break at $R = 25.2$, where our survey is 70% as efficient as its maximum efficiency. The result can be seen in Figure 8; it shows that the Petit et al. (2006) result is rejected at the 2σ level.

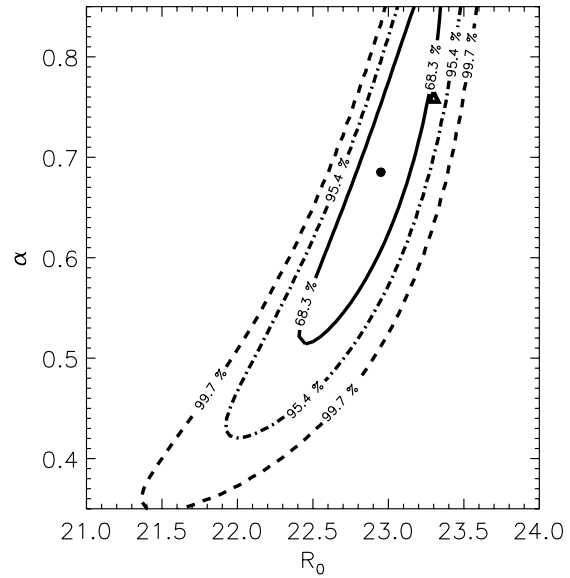


Figure 7. Contours of the SPL likelihood function for our sample limited to $R \leq 24.5$. The maximum likelihood point is marked with a dot ($\alpha = 0.69$, $R_0 = 23.0$). Marked with a triangle is the best value for the parameters based on Petit et al. (2006). Both results consistent with each other. This shows that our survey agrees with previous surveys if we consider only the range of magnitudes to which those surveys are sensitive.

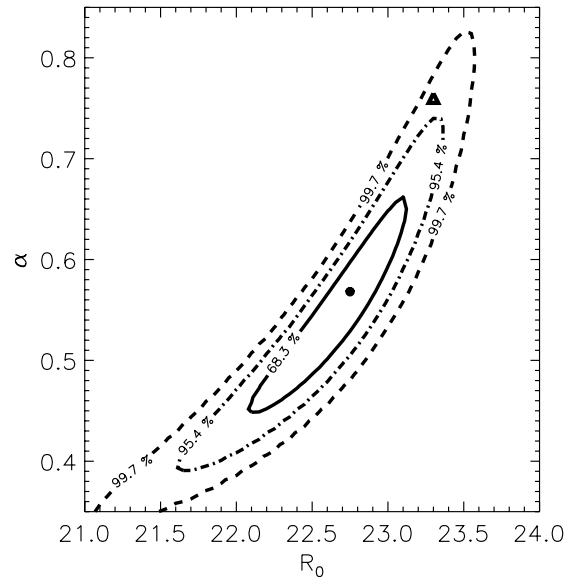


Figure 8. Contours of the SPL likelihood function for our sample limited to $R \leq 25.2$, where our survey is 70% efficient. The maximum likelihood point is marked with a dot ($\alpha = 0.57$, $R_0 = 22.8$) and the triangle is the Petit et al. (2006) result. We see that both results are inconsistent at more than a 2σ level. This demonstrates that our result does not rely on the detection of objects at magnitudes where our detection efficiency is declining.

5.3. Double Power Law Model

Now we have shown that our results are not well modeled by an SPL; we test a more complicated model. Any model that includes a break in the surface density distribution will have more free parameters than an SPL. Alternatives with three and four parameters were tried by Bernstein et al. (2004) to explain the aforementioned under-abundance of detections. We will focus on the “DPL” model, the harmonic mean of two different

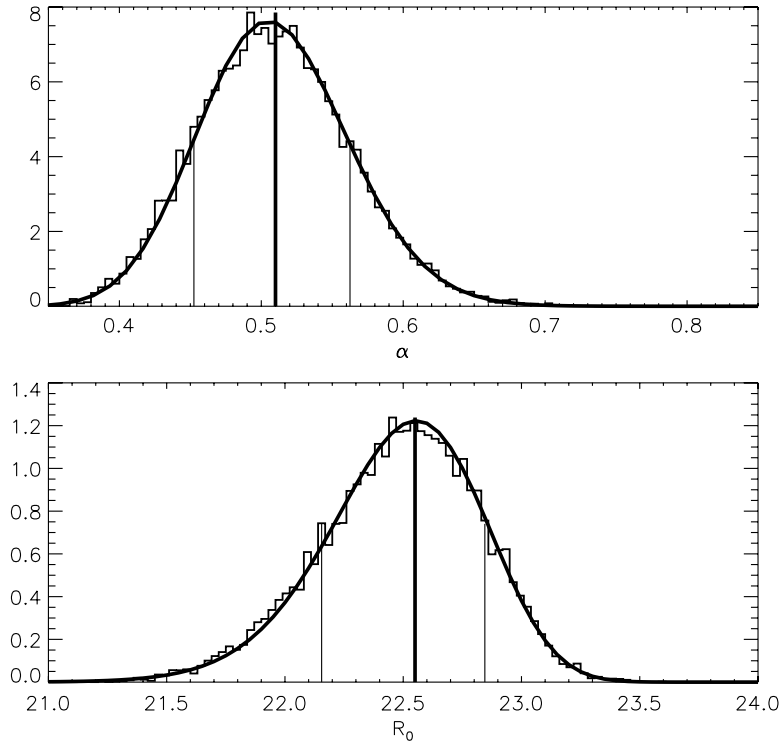


Figure 9. The probability density function for α and R_0 from the MCMC simulation is shown as a histogram. The likelihood function in Figure 6, shown as the marginal probability over each parameter is plotted as the solid curve. The solid, heavy line indicates the global maximum obtained by the MCMC run and the thin lines indicate the 1σ credible region of the parameter, inside of which we find 68.3% of the probability.

power laws. Though a model with three parameters would be easier to implement, it does not provide the immediate insight into the TNO population that the DPL provides. The DPL has four free parameters, allowing two different asymptotic power law behaviors for the distribution (that can be linked to the size distribution of small and large objects), a break in the luminosity distribution, and a differential density constant.

The larger number of parameters makes the likelihood function more difficult to sample; thus we use a Markov Chain Monte Carlo (MCMC) approach (for an MCMC review see Tegmark et al. 2004). We use a Metropolis–Hastings algorithm to sample the likelihood function with a Gaussian proposal distribution. The parameters were set to yield a $\sim 25\%$ acceptance rate. We considered a run of 100,000 iterations. To check for consistency we tried different initial conditions and compared the results, no disagreement was found. We also checked the performance of our MCMC code with the SPL model. In Figure 9 we show the marginalized probability for both parameters α and R_0 from MCMC and the exact result. There is evident agreement between the two approaches.

The DPL likelihood function is obtained by replacing the corresponding surface number density (Equation (10)) in the likelihood function (Equation (5)) with

$$\sigma_2(R) = C[10^{-\alpha_1(R-23)} + 10^{(\alpha_2-\alpha_1)(R_{\text{eq}}-23)-\alpha_2(R-23)}]^{-1},$$

$$C = \sigma_{23}(1 + 10^{(\alpha_2-\alpha_1)(R_{\text{eq}}-23)}). \quad (10)$$

In Figure 10 we show the DPL likelihood as a function of the bright-end slope α_1 , the faint-end slope α_2 , the value of the surface number density at $R = 23$ σ_{23} , and the break magnitude R_{eq} . All parameters but α_1 are well constrained by the data.

Given the small number of bright TNOs detected in our survey, the limited constraint on α_1 is not surprising.

5.4. Cumulative Number Density

Using the detection efficiency (Equation (2)) we can estimate the number of objects we missed for each object found. We construct a cumulative function of the unbiased population plotting each object individually, representing with its detection a number of objects with similar magnitudes. Since we plot a cumulative function, the errors are correlated (see Figure 11).

We go on to compare the total likelihood of both models, as described in Section 5.1. A simple way of doing this is to examine the goodness-of-fit of the cumulative number density. Figure 11 shows the data and the best solution for the SPL and DPL cases. Note that these power laws correspond to the cumulative number densities, $\Sigma_1(R) = 10^{\alpha(R-R_0)}$ and $\Sigma_2(R) = \int_{-\infty}^R \sigma_2(x) dx$.

It is expected that a DPL gives a better fit to the data than an SPL model. The question is whether this better fit overcomes the increased complexity in the model. This can be answered by calculating the quotient of the total Bayesian probabilities of the models (Bayes factor, details in Appendix 5.1). If the total probability for a given model is larger than another then it is preferred. Using the results of the MCMC simulations we compute this factor. The resulting total probabilities depend on suitable priors that reflect our ignorance on the parameters. We selected uniform priors for all our variables. For the SPL we chose $\alpha \in [0.35, 0.85]$, $R_0 \in [21.0, 24.0]$, while the DPL priors were uniform, $\alpha_1 \in [0.5, 1.0]$, $\alpha_2 \in [0.1, 0.7]$, $\sigma_{23} \in [0.5, 5.0]$, $R_{\text{eq}} \in [23.0, 26.0]$. The calculated Occam's factor is $O_{\text{sd}} = 26$, meaning that a DPL model is more likely to be a better representation for the brightness distribution of our data.

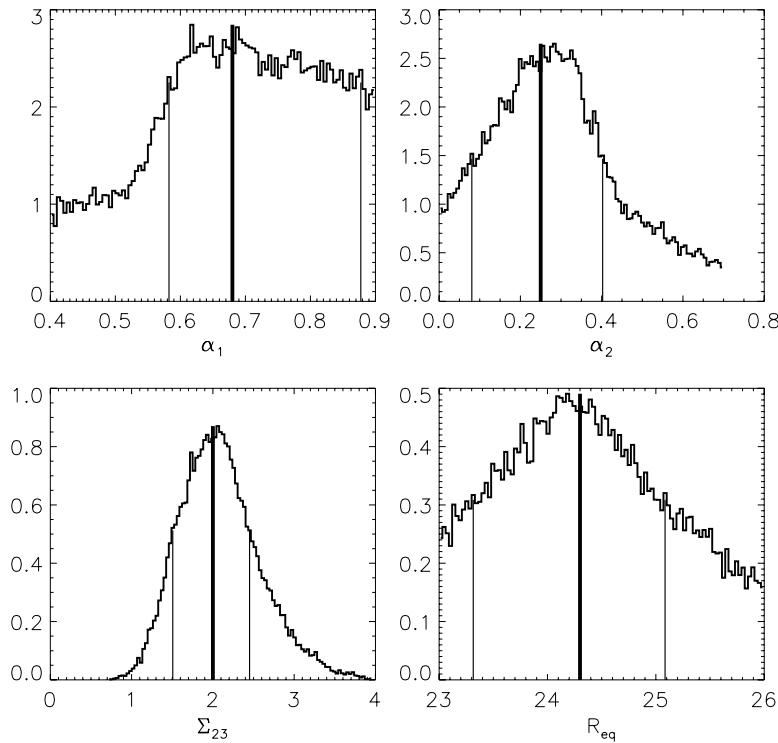


Figure 10. The DPL likelihood for our survey as a function of all parameters is shown in each window. The most likely parameters and their 1σ confidence regions, represented by the solid, heavy line and the two thin lines, are $\alpha_1 = 0.7^{+0.2}_{-0.1}$, $\alpha_2 = 0.3^{+0.2}_{-0.1}$, $\Sigma_{23} = 2.0^{+0.5}_{-0.5}$, and $R_{eq} = 24.3^{+0.8}_{-0.1}$.

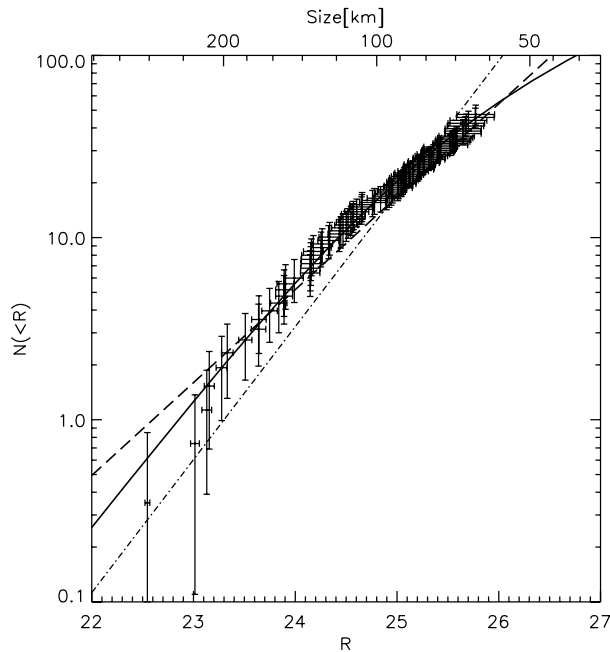


Figure 11. The cumulative number density for our survey. The best previous model is plotted in the short-dashed line. Our most likely solution for the SPL is plotted in the long-dashed line. The best DPL fit is shown as a solid line. The quoted size corresponds to an object at 42 AU and 4% albedo.

5.5. Other Surveys

Bernstein et al. (2004) combined the results of their *HST* survey with those of Chiang & Brown (1999), Gladman et al. (1998), Allen et al. (2002), Trujillo et al. (2001), Larsen et al. (2001), and Trujillo & Brown (2003). We include most of the

objects listed in that work and those conducted since. Table 2 differs from Bernstein et al. (2004, Table 2) in the exclusion of the two widest searches and the inclusion of two newer surveys (Petit et al. 2006; Fraser et al. 2008), as well as ours. We excluded the two surveys because of the complexity in establishing the searched area near the ecliptic. For the sake of comparison with Bernstein et al. (2004) we used the same criteria regarding detected objects as well as the caveats provided therein. We included surveys for which the location of the searched area, effective area of the search, magnitude at which the efficiency drops by 50% must be given. We included objects that have an observed magnitude where their efficiency function is more than 15% the maximum efficiency of the survey. We point out that all our detections satisfy this requirement.

We are interested in computing the likelihood of a model given the data from each survey. For this we only need the list of objects that meet our criteria, an estimate of the efficiency function, the surveyed area, and a way to translate all measurements to the red filter R for each survey. We use the approximation given in Equation (6). Figure 12 shows the 333 objects that we considered. It shows the existence of a very pronounced lack of detections at faint magnitudes. Our likelihood analysis is summarized in Figure 13 with 1σ confidence limits for the parameters.

An interesting aspect of our search is that the data have been available since 2003 August. Our survey's most likely distribution expects ~ 12 detections for the *HST* field while three were found. This provides independent support to the existence of a break in the TNO luminosity function.

5.6. Classical and Excited Population

We use the criteria in Bernstein et al. (2004) to identify “Classical” and “Excited” objects. TNOs with distance at

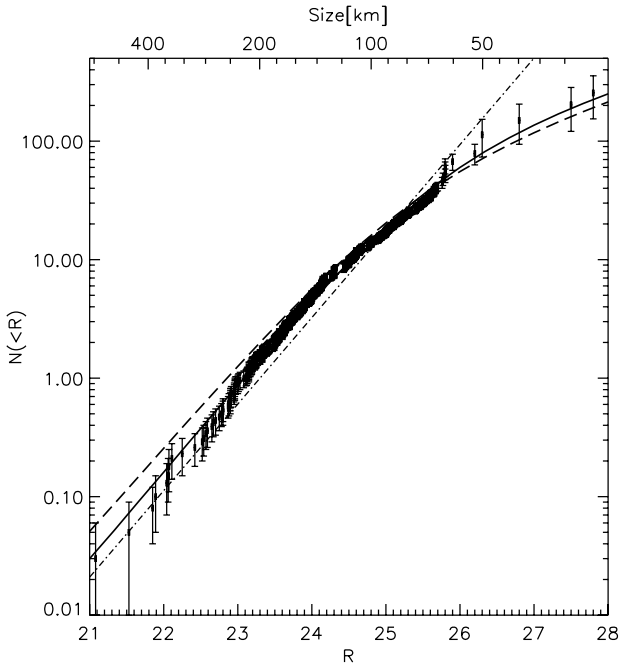


Figure 12. The cumulative number density for all surveys in Table 2. The best previous model is plotted in the black dashed line. Our most likely DPL is plotted in the long-dashed line. The most likely DPL (see Figure 13) considering all surveys is plotted as a full line. The apparent bump in density at around $R \sim 25.8$ corresponds to five objects in Gladman et al. (2001).

discovery d between 38 AU and 55 AU and inclination $i \leq 5$ deg are considered “Classical” and the rest are considered “Excited.” In Table 2 we list each survey with the corresponding number of TNOs in each category.

This survey was considered by itself and together with the surveys in Table 2. We investigated how does the DPL luminosity function change when applied to the different populations. We repeated the MCMC analysis for both populations and for our survey and the combined survey. We also considered the priors used in Bernstein et al. (2004), $-0.5 < \alpha_1, \alpha_2 < 1.5$ to constrain the parameter space.

The results of the MCMC simulations are summarized in Table 3. These results are very similar to those of Bernstein et al. (2004). However, we have included three new surveys (this survey and those of Petit et al. 2006 and Fraser et al. 2008), two of which (this survey and that of Fraser et al. 2008) sample magnitudes fainter than $R \sim 25.5$ where excited objects were specially undersampled.

5.7. Size, Distance, and Inclination Distribution

The size distribution is closely related to the distribution of apparent magnitudes. It is customary to assume all objects are located at the same distance and that the size distribution is an SPL and hence the cumulative brightness distribution is also a power law. The parameters of the two distributions are related by $q = 5\alpha + 1$, where q is the exponent of the differential size distribution ($dn = D^{-q}dD$) and α is the exponent of the SPL cumulative luminosity function.

With our rough distance estimates and assuming a 4% albedo for TNOs, we can compute the real size distribution of the objects in our survey (we adopt $m_R = -27.6$ for the R -band magnitude of the Sun). In Figure 14 we show the cumulative size distribution for our survey. However, the typical error in distance $\sim 7\%$ translates into a 0.3 mag photometric error, triple the median photometric error in our survey (see Figure 3). Thus, instead of repeating the statistical analysis for the size distribution directly, we transform our luminosity function into

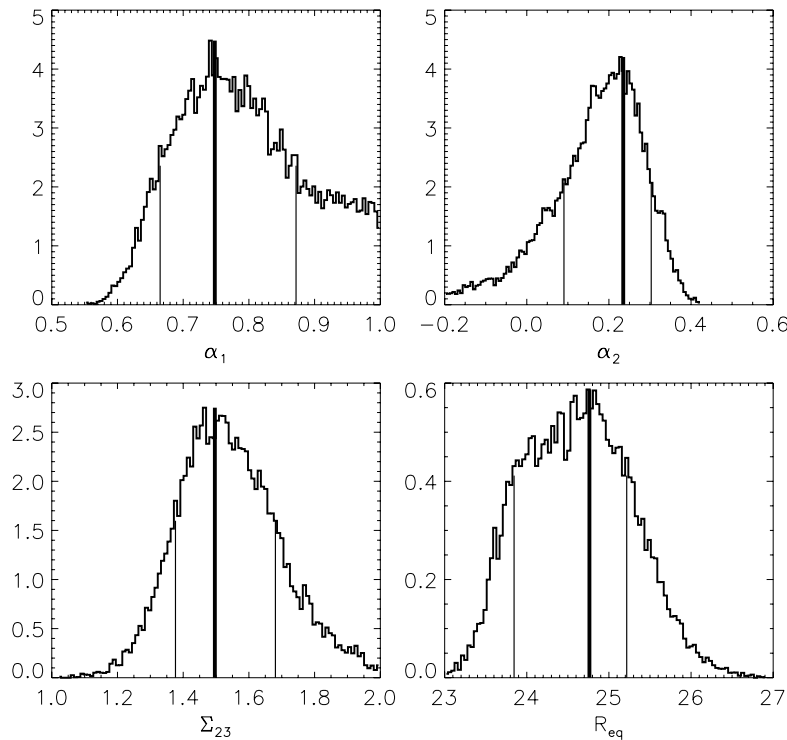


Figure 13. The DPL likelihood function marginalized over each parameter for all the surveys in Table 2. We see the maximum and 68% confidence region. The most likely value for each parameter and 1σ confidence limits are: $\alpha_1 = 0.75^{+0.12}_{-0.08}$, $\alpha_2 = 0.23^{+0.07}_{-0.14}$, $\Sigma_{23} = 1.50^{+0.18}_{-0.12}$ and $R_{eq} = 24.8^{+0.5}_{-0.9}$.

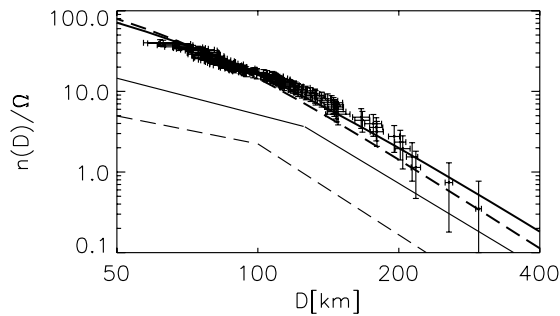


Figure 14. Number of TNOs observed in 1 deg² as a function of size. The solid line shows the model based on our survey. The dashed line is the model that considers all surveys. Both models are properly scaled to match the density observed in our survey.

Table 2
Surveys^a

Paper	Ω deg ²	R_{50}	N_C^b	N_E^b	N_{obs}	N_{exp}
Chiang & Brown (1999) ^c	0.01	27.0	1	1	2	1
Gladman et al. (2001) ^d	0.322	25.9	7	8	15	15
Trujillo et al. (2001) ^e	28.3	23.7	38	27	71	64
Allen et al. (2002)	2.30	25.1	15	15	30	39
Bernstein et al. (2004)	0.019	28.5	3	0	3	5
Petit et al. (2006) N	5.88	24.2	6	21	27	22
Petit et al. (2006) U	5.97	24.6	16	20	36	34
Fraser et al. (2008)	3.0	20.8	36	31	67	74
This survey ^e	2.83	25.69	54	18	82	74

Notes.

^a Details of the surveys considered in this work. Ω is the total surveyed area. R_{50} defines the R magnitude at which the survey's detection efficiency is 50% its maximum efficiency. The total number of objects discovered that had magnitude brighter than that at which the survey is 15% its maximum efficiency is N_{obs} , as defined in Bernstein et al. (2004). The expected number of objects for each survey given our most likely DPL luminosity function model for all surveys combined (see Figure 13) is N_{exp} .

^b Objects with inclination $i \leq 5$ deg and at a distance $38 \text{ AU} < d < 55 \text{ AU}$ are considered as Classical N_C and the rest as Excited N_E .

^c Based on Table 3 and comments in Gladman et al. (2001).

^d Based on Table 2 and comments in Bernstein et al. (2004).

^e In the Classical and Extended classification we only considered objects for which there was distance and inclination information.

Table 3
DPL Parameter Estimation^a

Survey		α_1	α_2	σ_{23}	R_{eq}
All surveys	TNO	$0.75^{+0.12}_{-0.08}$	$0.23^{+0.07}_{-0.14}$	$1.50^{+0.18}_{-0.12}$	$24.8^{+0.5}_{-0.9}$
	Classical	$1.4^{+0.1}_{-0.3}$	$0.32^{+0.04}_{-0.06}$	$0.82^{+0.13}_{-0.12}$	$23.3^{+0.3}_{-0.3}$
	Excited	$0.61^{+0.07}_{-0.05}$	$-0.3^{+0.4}_{-0.2}$	$0.68^{+0.09}_{-0.08}$	$25.7^{+0.7}_{-0.6}$
This survey ^b	TNO	$0.7^{+0.2}_{-0.1}$	$0.3^{+0.2}_{-0.2}$	$2.0^{+0.5}_{-0.5}$	$24.3^{+0.8}_{-0.1}$
	Classical	$1.2^{+0.3}_{-0.4}$	$0.15^{+0.20}_{-0.15}$	$1.5^{+0.5}_{-0.5}$	$23.6^{+0.6}_{-0.7}$

Notes.

^a Best-fit parameters and 1σ confidence limits based on MCMC simulations. All surveys are detailed in Table 2.

^b In this survey there were only 18 excited objects, too few to constrain a four-parameter model. However we could fit an SPL with $\alpha = 0.62 \pm 0.12$ and $R_0 = 24.2 \pm 0.3$ to this population.

a size distribution assuming all objects are located at 42 AU. The best DPL fits for the luminosity function are plotted as a function

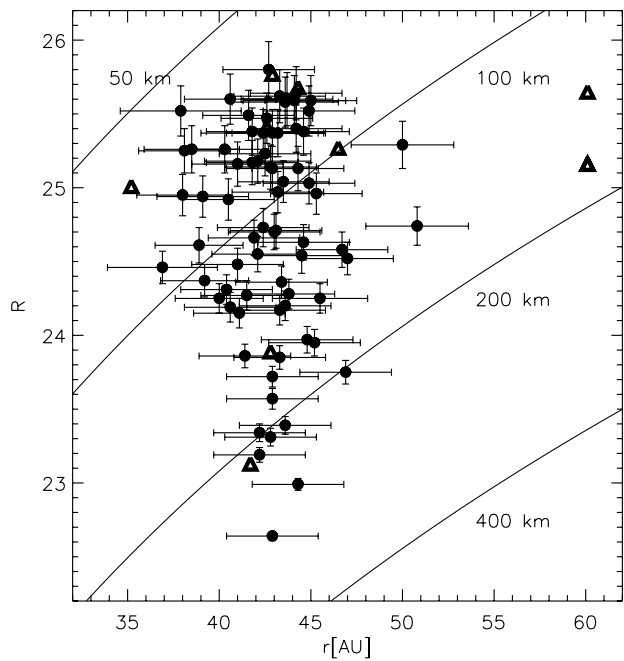


Figure 15. Magnitude and distance for all 82 TNOs found. The black dots are objects observed in both nights and the triangles are those with only one night's observation. We assume a 4% albedo to plot the constant size curves for 100, 200 and 400 km in black.

of size. The solid line is the fit to this survey and the dashed line corresponds to the fit to the surveys in Table 2. We also consider a toy model based on the DPL; it corresponds to two power laws with indices $q_1 = 5\alpha_1 + 1$ and $q_2 = 5\alpha_2 + 1$ that are joined at the size for which an object at 42 AU would be observed to have magnitude R_{eq} . We plot the cumulative function of the toy models for both DPLs to show the asymptotic behaviors as a light solid line and a light dashed line respectively, both arbitrarily offset vertically for clarity. In Figure 14 there is a clear agreement between the real size distribution and the fit for the DPL models indicates that the assumption that all TNOs are at the same distance is justified.

In Figure 15 we plot the distance and magnitude for each object. The distance corresponds to d_{bary} in Table 1 with the exception of those objects that were not recovered on the second night for which we plot the circular orbit approximation (d_{par}). We consider only the subset of 73 objects with 24 h arcs data, with a distance error of 5%.

All but two objects are located at less than 50 AU from the Sun, although we are able to detect $D = 250 \text{ km}$ TNOs at distances of 80 AU, with 50% efficiency. This lack of distant detections has been noted previously (Allen et al. 2001; Trujillo et al. 2001; Bernstein et al. 2004) with the recurrent hint that there is an “edge” to the Kuiper belt.

Given the size distribution that corresponds to our best fit luminosity function we are able to calculate the distance bias in our sample and obtain the real distance distribution. We follow the approach of Trujillo et al. (2001). The true and observed distributions are related by $f(r)dr \propto \beta(r)f_o(r)dr$, where $\beta(r)^{-1} = \int_{r_0}^r n(D)dD$ is the bias factor and $n(D)$ is the TNO size distribution. This is done for 10 magnitude bins between 22nd and 26th magnitude and independent estimates of the bias function are obtained. We used the average to test the effect of the DPL size distribution to the distance distribution of objects, as shown in Figure 16. We see an abrupt drop in the abundance

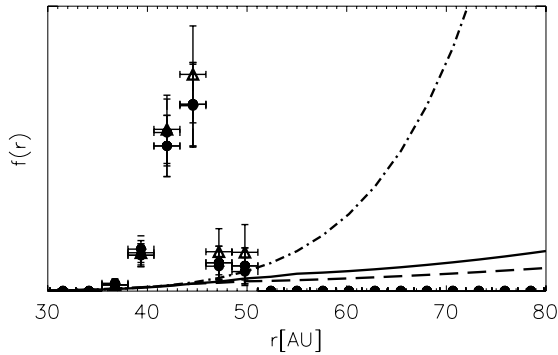


Figure 16. Shape of the debiased distance distribution of TNOs assuming a constant albedo = 4%. The triangles assume a size distribution with a power law of index $q = 4$. The dark points assume the DPL size distributions. The bias corrections β are overplotted as a dot-dashed line for an SPL with exponent $q = 4$, a solid line for a broken power law based on our survey and as a dashed line for parameters based on all surveys combined.

of objects at $r \sim 47$ AU, regardless of the size distribution considered, as has been described by others (Trujillo et al. 2001; Petit et al. 2006). However, a DPL size distribution gives a much tighter constraint on the existence of a distant population. This is due to its much shallower size distribution for small bodies as can be seen in the bias correction for the DPL for our survey and the one for all surveys.

Given the fact that we detect no objects farther than 50 AU we can constrain the surface density Σ of a different population located outside 50 AU. At 95% confidence level, the detection of no objects is consistent with an expectation of three detected objects. We calculated this for the observed population $N_{\text{exp}} = \Omega \int_0^\infty \eta(x) \Sigma(x) dx$, where η is the detection efficiency of our survey. We assume for simplicity that the size distribution of the distant population is the same as what we have measured for the objects in our survey. We will also assume that each object in the population is shifted to larger heliocentric distances by the same factor. It is useful to define the limit on a distant population at distance d as the maximum fraction of the observed population's surface density that a population can have to be consistent with no detections. We denote this fraction as $g(d)$, following the notation in Bernstein et al. (2004). For 60 AU we find $g = 0.08$, compared to $g = 0.17$ found by Bernstein et al. (2004). Our survey rejects another population with the same mass closer than 110 AU. Thus, we place a tight limit on the existence of a distant population. We support the conclusion of Bernstein et al. (2004) that if such a population exists, it is either substantially less massive than the observed classical Kuiper belt or it is comprised of small bodies that are beyond our detection threshold.

Using the inclination information in Table 1 we can show the inclination distribution for the objects in our survey. The results are shown in Figure 18. This is very similar to the results in Brown (2001).

5.8. Mass

We use the results of our MCMC analysis to estimate the total mass of TNOs to which our survey is sensitive. At each step in the MCMC runs, we compute the mass that corresponds to the DPL parameters (again, assuming a heliocentric distance of 42 AU and a geometric albedo of 0.04). We follow the

parameterization used in Bernstein et al. (2004):

$$M_{\text{tot}} = M_{23} \Omega \int \sigma(R) 10^{-0.6(R-23)} dR f^{-1} \left[\frac{\rho}{1000 \text{ kg m}^{-3}} \right] \times \left[\frac{d}{42 \text{ AU}} \right]^6 \left[\frac{p}{0.04} \right]^{-3/2}, \quad (11)$$

where $M_{23} = 6.3 \times 10^{18} \text{ kg} = 1.055 \times 10^{-6} M_{\oplus}$ and f is the fraction of objects from the given population that are located within Ω .

We consider the complete TNO population and the Classical and Excited sub-samples. The DPL size distribution allows us to compute the value of the integral in Equation (11); however the total mass of a given population depends heavily on the mean values of the assumed physical parameters. The mass probability distribution is calculated assuming all other parameters are fixed. The uncertainties on the rest of the parameters (density, albedo, distance, and fraction in the surveyed area) can be accounted for independently. We considered an effective area of ± 3 deg from the ecliptic, giving $\Omega = 21,600 \text{ deg}^2$ and that all objects in each population are located within that area ($f = 1$). We have also assumed mean albedo $p = 0.04$, distance $d = 42 \text{ AU}$, and density $\rho = 1000 \text{ kg m}^{-3}$.

In Figure 17 the mass distribution is plotted for our survey alone (solid lines) and for the combination of all the surveys listed in Table 2 (dot-dashed lines). In black we show the entire TNO sample. The most probable mass in TNOs for the combination of all surveys is $M_{\text{tno}} = 0.020^{+0.004}_{-0.003} M_{\oplus}$ while for our survey alone we obtain $M_{\text{tno}} = 0.025^{+0.016}_{-0.007} M_{\oplus}$. These are consistent with each other and with the previous estimate by Bernstein et al. (2004). This is not surprising since most of the mass is present in TNOs with sizes comparable to the size at which the distribution breaks. The slight overabundance of TNOs in our survey with respect to other surveys yields a higher mass for the TNO population. It is important to note that in Equation (11) the total mass diverges if either $\alpha_1 < 0.6$ or $\alpha_2 > 0.6$. We also see in Figure 17 that for the results of our survey alone there is a long tail to higher masses. This is due to the poor constraint on the bright end of the TNO luminosity function given the limited areal coverage of our survey (2.83 deg^2). However, the combination of all surveys yields a better constraint, and we obtain convergent masses for all steps in our MCMC run.

When we consider the Classical and Excited populations separately the mass distributions change. In Figure 17 we show the mass in Classical objects in green and that in Excited objects in red. Using all the surveys the mass in classical objects is very well constrained to be $M_{\text{cla}} = 0.008 \pm 0.001 M_{\oplus}$. Based on our survey alone, we find $M_{\text{cla}} = 0.013 \pm 0.003 M_{\oplus}$. The overabundance of Classical objects in our survey is responsible for that seen in the entire TNO population.

The mass in Excited objects using all surveys is $M_{\text{exc}} = 0.010^{+0.021}_{-0.003} M_{\oplus}$, larger than that found for the Classical TNOs, and is also less well constrained, with a long tail to higher masses. This reflects the relatively poor constraint on the size distribution of Excited objects, where the limits are set by what values for the exponent of the power-law size distribution are considered to be physically plausible. With only 18 Excited objects in our survey we have a very poor constraint on the individual DPL parameters. However, the mass is well constrained. We find $M_{\text{exc}} = 0.005^{+0.004}_{-0.003} M_{\oplus}$, less than the mass in Classical TNOs. This is due to the relative under-abundance of Excited objects in our survey. This can be explained by the fact

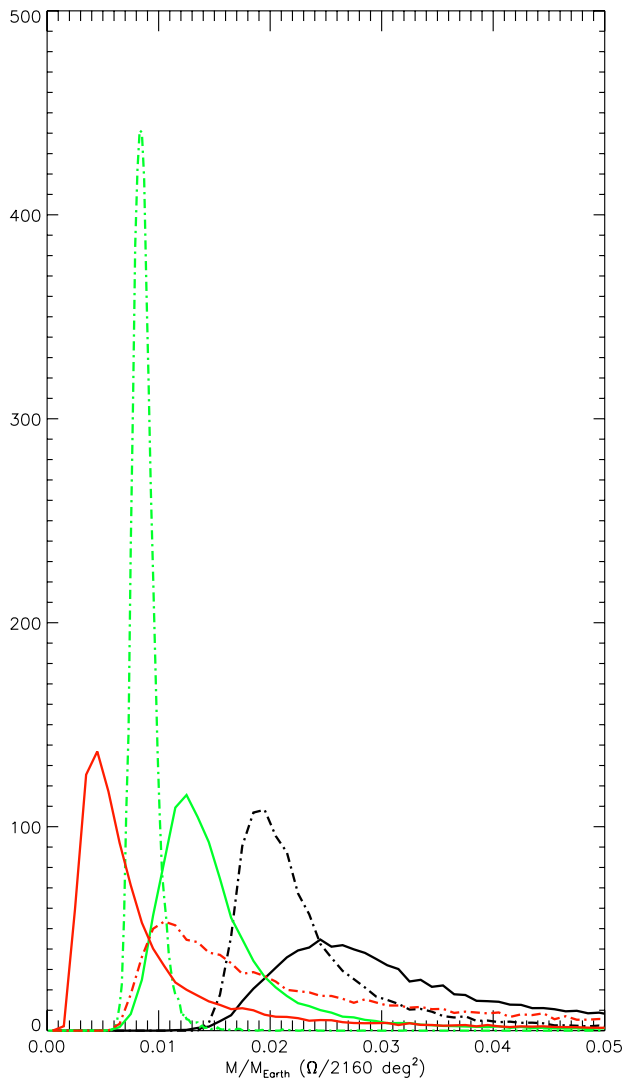


Figure 17. Mass distribution for our population of TNOs. We extend our result over a solid angle of $360 \times 6 \text{ deg}^2$, assuming the fraction of the population that is within this solid angle f is 1. The solid lines represent the results from our survey alone while all surveys in Table 2 are shown as dot-dashed lines. The black lines correspond to the whole TNO sample; green and red are used for the Classical and Excited sub-samples, respectively.

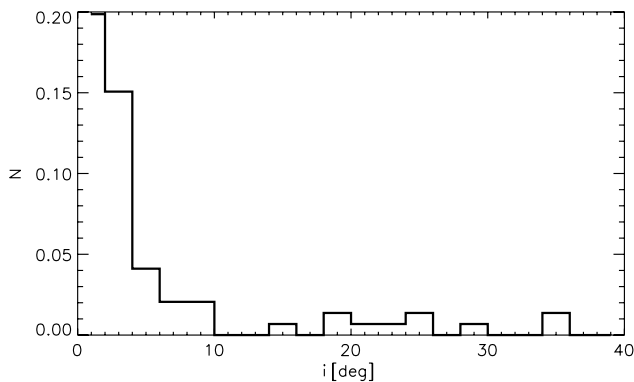


Figure 18. Inclination probability distribution of TNOs in our survey.

the survey was conducted in the direction of Uranus, separated about 18.5 deg from Neptune, where we expect Plutinos to be near apocenter and hence faint and under-represented.

6. CONCLUSIONS

We have presented a TNO survey that is both deep ($R_{50} = 25.6$) and broad ($\sim 2.8 \text{ deg}^2$), finding 82 TNOs. The survey is very well characterized and simple, reaching its limiting magnitude in single exposures.

We have studied the luminosity function of the TNOs in our survey. We found a significant deviation from an SPL behavior in the cumulative function at $R \sim 25$. We have shown that our data are consistent with an SPL, and with many other shallower surveys, if we consider only objects brighter than $R = 24.5$. We have also demonstrated that the apparent deviation from an SPL is not an artifact of our detection efficiency.

Whether our data support a break in the luminosity function is a matter of statistical analysis. We compared two models, one where the distribution increases exponentially with an SPL and one where there are two different slopes in the sampled magnitude region, and compute the total probability of each model with Bayesian statistics (Gregory 2005) (see details in Section 5.1). The ratio of the total likelihood for a DPL and an SPL model is ~ 26 . This can be interpreted as the DPL model being 26 times more probable than the SPL given our data set.

We conclude that our survey provides significant evidence for a break in the TNO luminosity function. This is the first survey that is able to make such a claim without relying upon the results of other surveys. Our result is easy to interpret since we do not have to make assumptions about the distribution of objects in different parts of the sky. Nonetheless, the comparison with other surveys is fundamental since there are published searches that sample the same magnitude region. We have considered most of the published data up to 2007 July regarding surveys of the trans-neptunian space in the same spirit of Bernstein et al. (2004). Again, our DPL model accurately describes the cumulative number density for all surveys combined.

Only two ground-based surveys are as deep as the present one, and they have not seen a significant deviation from an SPL. The survey of Gladman et al. (2001) covered much less area and, consequently, discovered many fewer TNOs in this magnitude range (17 objects for the entire survey). Given the small numbers, our results are not inconsistent with those of Gladman et al. (2001). Fraser et al. (2008) report the combined results of surveys taken at different ecliptic latitudes and longitudes. They fit for an SPL but account for variations in the sky surface density, which may be due to surveying at different ecliptic longitudes and latitudes, by allowing an offset in the luminosity function zero point for each survey. This substantially increases the number of free parameters and, we believe, allows deviations from an SPL within individual surveys to be obscured when the results of several surveys are combined. We believe that this explains the difference between the present results and those of Fraser et al. (2008).

We make the assumption that all objects are located at the same distance, so the luminosity function can be translated into a size distribution. For every object with a reliable distance estimate a nominal size can be computed (we assume an albedo of $p = 0.04$). The size distribution of our survey was compared with the single distance approximation and we showed they agree. We then interpret the DPL size distribution.

The break in the size distribution reflects the size at which collisional processes take over gravitational ones. This is, the largest object that is expected to be disrupted in a collision in the age of the solar system. The best DPL model for our survey features a break at $D = 130(p/0.04)^{-0.5} \text{ km}$ bodies while for

all surveys it is at $D = 100(p/0.04)^{-0.5}$ km. Current models expect the break to occur at smaller sizes, $D \leq 50$ km for Pan & Sari (2005) and $D \leq 100$ km for Kenyon & Bromley (2004). We consider these models to be consistent with our result given the assumptions on poorly constrained quantities like the albedos on the observational side as well as initial conditions in the theory are not well constrained. The effect of a distribution of albedos and a possible correlation with object size and heliocentric distances should be studied.

The inclination distribution for our survey is consistent with what is expected from previous results (Brown 2001). However, we do not have enough objects to do a detailed study of the distribution. We do, however, separate our population into classical (“cold”) and excited (“hot”) objects. We study the size distribution of these samples and find them to show differences as done previously by Bernstein et al. (2004).

We calculate the probability distribution for the total mass in TNOs, Classical and excited objects that are consistent with our observations and all considered surveys. For all surveys combined we find $M_{TNO} = 0.020^{+0.004}_{-0.003} M_{\oplus}$. It is interesting to note that for the Classical population the mass is very well constrained to be $M_{cla} = 0.008 \pm 0.001 M_{\oplus}$ while the excited population gives a larger and poorly constrained mass of $M_{exc} = 0.010^{+0.021}_{-0.003} M_{\oplus}$. This provides evidence for a difference between the “hot” and “cold” populations. Our survey gives a consistent but slightly higher answer for Classical objects which we believe is due to the local overabundance of objects in our survey. We only have 18 excited objects in our sample, too few to constrain the parameters of the luminosity function, but enough to show there is an under-abundance of Excited objects in our survey. This is explained by the direction of our fields, close to where most of the Plutinos come to apocenter.

Given the size distribution we calculate a distance bias correction (Trujillo & Brown 2001). We then obtain the real distance distribution of objects, assuming we are just as likely to find faint objects that are close as those that are far. Our survey is very well suited to detecting objects that show slow parallactic movement (distant); our detection efficiency is essentially independent of rate for rates larger than $0.9'' \text{ h}^{-1}$ (distances closer than 150 AU). According to Dones (1997), Jewitt et al. (1998), and Trujillo & Brown (2001) the fraction h of objects found outside 48 AU should be about 40% for a population with a smooth brightness distribution that extends beyond 50 AU. In our sample there are 73 TNOs with reliable distance estimates, of which 71 are located between 30 AU and 47 AU, and only two at ~ 50 AU, accounting for $h = 3\%$. Once we take into account the biases associated with distance these numbers indicate an abrupt drop in the radial density of the Kuiper belt. If we also consider the size distribution break found in our sample we also rule out the existence of a far population of TNOs near the plane of the ecliptic. We have found more evidence for an edge of the Classical belt population at around 47 AU and placed a constraint on the surface density of objects for an unseen population at 60 AU of 8% that of the observed Classical belt. We also set a minimum distance for a “belt-like” population with the same mass as that of the Classical belt of 110 AU.

Deeper surveys will help better constrain where the break in the luminosity function occurs and complete the picture of the trans-Neptunian space. The size distribution would be better determined if these surveys are also careful in obtaining follow-up observations to measure accurate distances for faint objects.

We are grateful to Charles Alcock, Scott Kenyon, and David Latham for their comments and suggestions. We thank the anonymous referee for a very helpful and informative review. We thank Matthew R. George for helpful conversations and for his assistance in modifying the Bernstein & Khushalani (2000) *Orbfit* routines. This work was supported in part by NASA grant NNG04GK64G, issued by the NASA Planetary Astronomy Program.

REFERENCES

- Alard, C. 2000, *A&AS*, **144**, 363
 Allen, R. L., Bernstein, G. M., & Malhotra, R. 2001, *ApJ*, **549**, L241
 Allen, R. L., Bernstein, G. M., & Malhotra, R. 2002, *AJ*, **124**, 2949
 Bernstein, G., & Khushalani, B. 2000, *AJ*, **120**, 3323
 Bernstein, G. M., Trilling, D. E., Allen, R. L., Brown, M. E., Holman, M., & Malhotra, R. 2004, *AJ*, **128**, 1364
 Bertin, E., & Arnouts, S. 1996, *A&AS*, **117**, 393
 Brown, M. E. 2001, *AJ*, **121**, 2804
 Brunini, A., & Fernandez, J. A. 1996, *A&A*, **308**, 988
 Chiang, E. I., & Brown, M. E. 1999, *AJ*, **118**, 1411
 Cutri, R. M., et al. 2003, IRSA 2MASS All-Sky Point Source Catalog, (NASA/IPAC Infrared Science Archive) <http://irsa.ipac.caltech.edu/applications/Gator/>
 Dones, L. 1997, in ASP Conf. Ser. 122, From Stardust to Planetesimals, ed. Y. J. Pendleton (San Francisco, CA: ASP), 347
 Elliot, J. L., et al. 2005, *AJ*, **129**, 1117
 Fraser, W. C., et al. 2008, arXiv:0802.2285
 Gladman, B., & Kavelaars, J. J. 1997, *A&A*, **317**, L35
 Gladman, B., Kavelaars, J. J., Nicholson, P. D., Lored, T. J., & Burns, J. A. 1998, *AJ*, **116**, 2042
 Gladman, B., Kavelaars, J. J., Petit, J.-M., Morbidelli, A., Holman, M. J., & Lored, T. J. 2001, *AJ*, **122**, 1051
 Gregory, P. C. 2005, in Bayesian Logical Data Analysis for the Physical Sciences: A Comparative Approach with “Mathematica” Support, ed. P. C. Gregory (Cambridge: Cambridge Univ. Press)
 Ichikawa, S.-I. 2002, *Astron. Herald*, **95**, 266
 Ida, S., Larwood, J., & Burkert, A. 2000, *ApJ*, **528**, 351
 Irwin, M., Tremaine, S., & Zytow, A. N. 1995, *AJ*, **110**, 3082
 Jewitt, D. 2003, *Earth Moon Planets*, **92**, 465
 Jewitt, D. C., & Luu, J. X. 1995, *AJ*, **109**, 1867
 Jewitt, D., Luu, J., & Marsden, B. G. 1992, *IAU Circ.*, **5611**, 1
 Jewitt, D., Luu, J., & Trujillo, C. 1998, *AJ*, **115**, 2125
 Kavelaars, J. J., et al. 2004, *Icarus*, **169**, 474
 Keller, S. C., et al. 2007, *PASA*, **24**, 1
 Kenyon, S. J., & Bromley, B. C. 2004, *Nature*, **432**, 598
 Kenyon, S. J., Bromley, B. C., O’Brien, D. P., & Davis, D. R. 2007, arXiv:0704.0259
 Kobayashi, H., & Ida, S. 2001, *Icarus*, **153**, 416
 Landolt, A. U. 1992, *AJ*, **104**, 340
 Larsen, J. A., et al. 2001, *AJ*, **121**, 562
 Larsen, J. A., et al. 2007, *AJ*, **133**, 1247
 Levison, H. F., & Duncan, M. J. 1990, *AJ*, **100**, 1669
 Millis, R. L., Buie, M. W., Wasserman, L. H., Elliot, J. L., Kern, S. D., & Wagner, R. M. 2002, *AJ*, **123**, 2083
 Miyazaki, S., et al. 2002, *PASJ*, **54**, 833
 Morbidelli, A., Levison, H. F., & Gomes, R. 2007, arXiv: astro-ph/0703558
 Pan, M., & Sari, R. 2005, *Icarus*, **173**, 342
 Peixinho, N., Boehnhardt, H., Belskaya, I., Doressoundiram, A., Barucci, M. A., & Delsanti, A. 2004, *Icarus*, **170**, 153
 Petit, J.-M., Holman, M. J., Gladman, B. J., Kavelaars, J. J., Scholl, H., & Lored, T. J. 2006, *MNRAS*, **365**, 429
 Petit, J.-M., Holman, M., Scholl, H., Kavelaars, J., & Gladman, B. 2004, *MNRAS*, **347**, 471
 Schechter, P., & Press, W. H. 1976, *ApJ*, **203**, 557
 Sheppard, S. S., Jewitt, D., & Kleyna, J. 2005, *AJ*, **129**, 518
 Tegmark, M., et al. 2004, *Phys. Rev. D*, **69**, 103501
 Trujillo, C. A., & Brown, M. E. 2001, *ApJ*, **554**, L95
 Trujillo, C. A., & Brown, M. E. 2003, *Earth Moon and Planets*, **92**, 99
 Trujillo, C. A., Jewitt, D. C., & Luu, J. X. 2001, *AJ*, **122**, 457
 Tyson, A., & Angel, R. 2001, in ASP Conf. Ser. 232, The New Era of Wide Field Astronomy, ed. R. Clowes, A. Adamson, & G. Bromage (San Francisco, CA: ASP), 347